Chapter 4 *Structure, Microstructure and Magnetic Properties of Hydrothermally Synthesized δ-MnO₂*

4.1 Introduction

Among all the polymorphs of MnO_2, one may find scarce of report on δ-MnO_2 although it plays a significant role in the transport and speciation in the natural environment due to their typical cation exchange capacity, sorptive, catalytic, and oxidative properties. Besides, δ phase has a large surface area. Over the past few years, efforts have been devoted to synthesize δ-MnO_2 nanostructures of different morphologies, such as nanoflakes [36], nanosheets [172][110], nanowall [173], nanorods [174]. Although δ-MnO_2 is knon to show antiferromagnetic behaviour [175], less focus has been paid towards its magnetic properties with varying shape and size. It is also possible to vary the magnetic properties after insertion of external cation, water molecule, or by creating cation vacancies within the layers of δ-MnO_2. The negative charge of cationic vacancies is compensated by the charge of the interlayer metal cations which could govern the magnetic coupling between Mn (Mn^{3+} and Mn^{4+}) cations.

In this chapter, we have successfully synthesized the pure phase of $P6_3/mnm$, δ-MnO_2 by facile hydrothermal technique at 120°C for 6 h. The structural and microstructural properties of the synthesized sample, characterized through X-ray diffraction, Fourier transform infrared spectroscopy, Raman spectroscopy, Transmission electron microscope and X-ray photoelectron spectroscopy are discussed in section 4.2. ac susceptibility along

with remanent magnetization measurements show the spin-glass behaviour of δ-MnO$_2$ are illustrated in section 4.3. Moreover, the structure of δ-MnO$_2$ with its magnetic behaviour and possible origin has been discussed in this chapter.

4.2 Structural and Microstructural Analysis

4.2.1 X-ray Diffraction

The X-ray diffraction pattern is shown in figure 4.1 demonstrates three pronounced peaks at 12.54°, 25.25°, and 36.22° corresponding to (001), (002), and (-111) of δ-MnO$_2$ (potassium birnessite) (JCPDS no. 80-1098). The broad nature of diffraction peaks signifies the presence of a low degree of crystallinity of δ-MnO$_2$. No peaks associated with the impurity phase are observed, suggesting the formation of pure δ phase of MnO$_2$. The crystallite size (D) is estimated through Scherrer equation, $D = k\lambda/\beta cos\theta$, where k = 0.9 is the Scherrer constant, λ is the wavelength of X-rays, β and θ are FWHM (full width half maxima) and peak position in radian, respectively. The estimated crystallite size for the most intense peak i.e. (001) is found to be ~ 5.3 nm. The basal plane spacing calculated from (001) plane is ~ 0.73 nm, which is the characteristic of δ-MnO$_2$ due to water molecules and intercalated potassium ions. The calculated interplanar spacing for (002), (-111), and (-112) are ~ 0.35nm, ~ 0.24 nm, and ~ 0.22 nm respectively which match well with the δ-MnO$_2$ JCPDS no. 80-1098.

4.2.2 Fourier Transform Infrared Spectroscopy

The functional group presents at the surface of the prepared δ-MnO$_2$ phase are characterized by using FT-IR spectroscopy as shown in figure 4.2. In the range of 500 to 4000 cm^{-1}, the main absorption bands are observed at 3511, 1673, 1373, 1174, and 825 cm^{-}

[1], respectively. The main absorption band at 3511 is attributed to Mn–OH stretching of the interlayer water molecules. The weak absorption band observed at around 1673 and 1174 cm^{-1} may correspond to the bending vibrations of the hydroxyl group (O–H) combined with Mn atoms from the absorbed water molecules. The peak appearing at around 1373 and 825 cm^{-1} are attributed to the surface –OH groups of the Mn-O-Mn bond in [MnO_6] octahedra, which further demonstrates the presence of MnO_2 phase [86][112]. Weak absorption bands observed at 2165, 2356, and 2944 cm^{-1} may be attributed to –CH group due to C-O stretching vibrations of ethanol used in the synthesis [176].
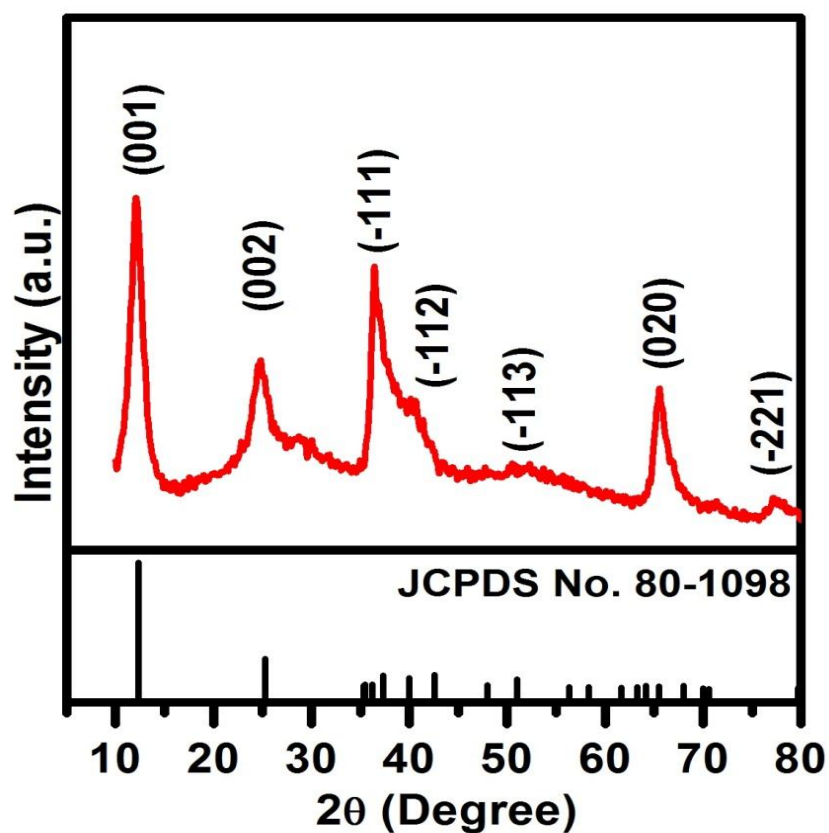

Figure 4.1: X-ray diffraction pattern of δ-MnO₂.

4.2.3 Raman Spectroscopy

Particularly, the vibrational feature of the birnessite-type MnO_2 structure is their low Raman activity. Three major features can be recognized at 500-510, 575-585, and 625-650 cm^{-1} in the Raman spectrum of δ-MnO_2 as shown in figure 4.3. Lower wavenumber band appears weak rather than the bands at high frequency region which dominates the whole spectra [177]. The nature of the ions present within the basal MnO_6 sheets is responsible for spectral modifications. The band at 642 cm^{-1} can be assigned to the symmetric stretching vibrations (Mn-O) of [MnO_6] octahedra while the band at 576 cm^{-1} is due to (Mn-O) stretching in the basal plane of [MnO_6] sheet [58].

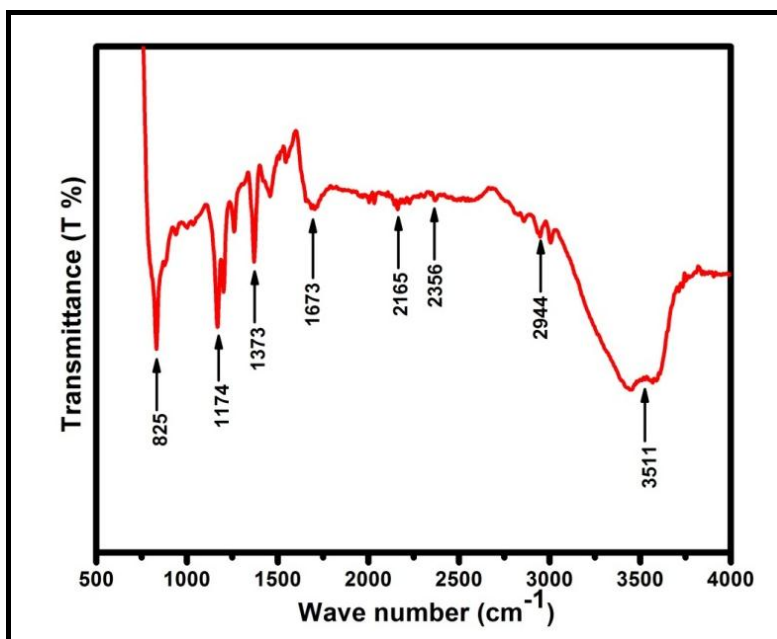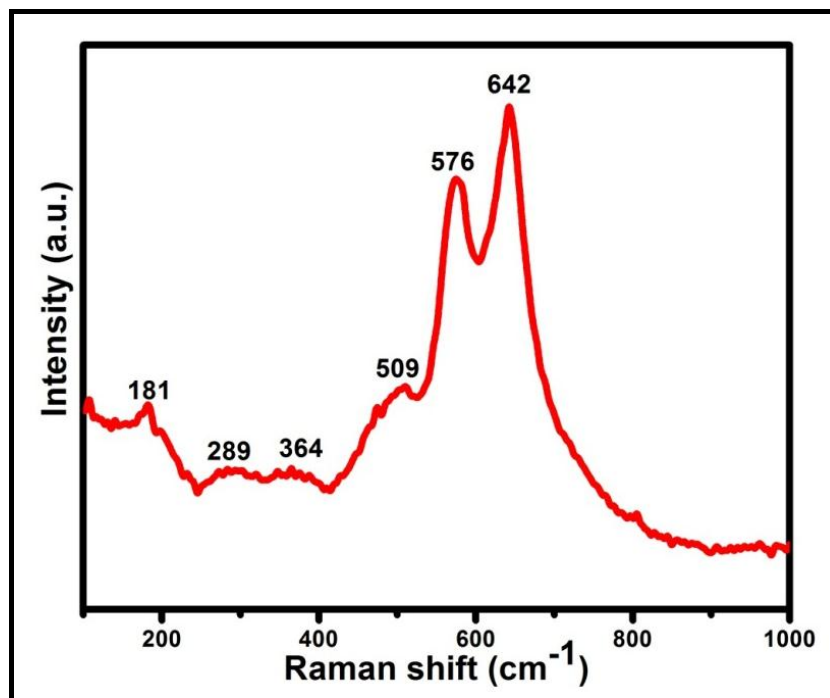**Figure 4.2:** *FTIR spectrum of δ-MnO_2.*

Figure 4.3: *Raman spectroscopy of δ-MnO₂.*

4.2.4 Transmission Electron Microscope

Transmission electron micrograph shown in figure 4.4(a) shows the formation of agglomerated nanorods of synthesised δ-MnO$_2$. The enlarge view of selected area is shown in figure 4.4(b). From high-resolution TEM as shown in figure 4.4(c), the interplanar spacing is estimated to be 0.37 nm and 0.28 nm corresponding to (002) and (-112) of monoclinic, δ-MnO$_2$ corroborates well with XRD results. Furthermore, the selected area electron diffraction (SAED) pattern demonstrates distinguished diffraction rings indexed as (002), (-112) and (020) corroborating with the XRD result (figure 4.4(d)). Therefore, we conclude here that through the hydrothermal technique, pure phase of δ-MnO$_2$ is formed which are confirmed through XRD, FT-IR, and Raman spectroscopy.
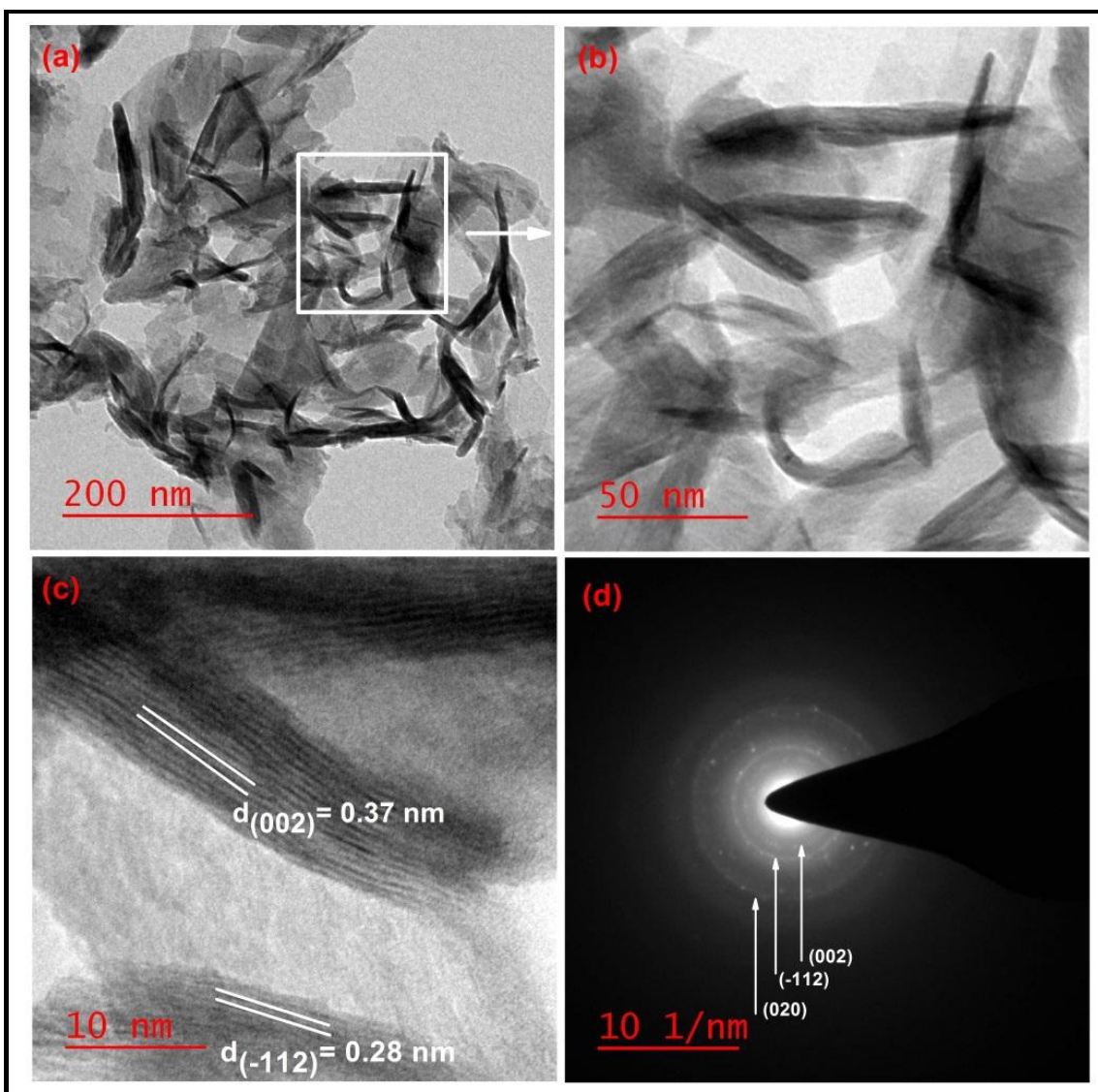
Figure 4.4: *(a) Low resolution and (b) high resolution image of Transmission electron micrograph of δ-MnO₂. Inset shows the particle size distribution histogram, (c) High resolution TEM and (d) SAED pattern of δ-MnO₂.*

4.2.5 X-Ray Photoelectron Spectroscopy

Figure 4.5 depicts the room temperature XPS spectrum of δ-MnO$_2$ fitted with Gaussian-Laurentz peak using software XPS peak 4.1 with straight background. All the peaks are calibrated with respect to the carbon 1s peak of binding energy 284.8 eV. Figure 4.5 (a)
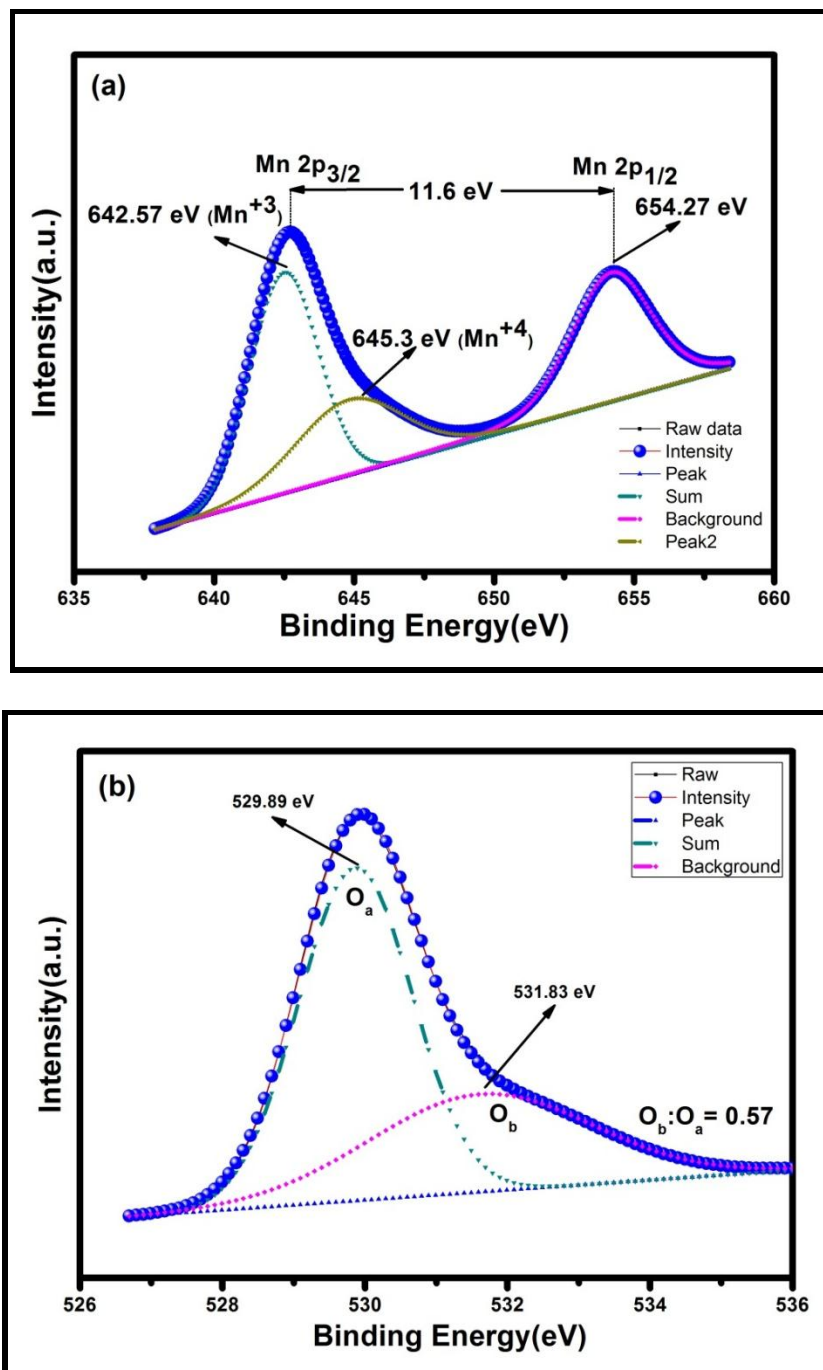
Figure 4.5: *X-ray photoelectron spectroscopy of (a) Mn 2p and (b) O 1s of δ-MnO₂.*

shows the Mn spectrum having two strong peaks ascribed to $Mn2p_{3/2}$ and $Mn2p_{1/2}$ focused at 642.72 and 654.27 eV, respectively. Further, $Mn2p_{3/2}$ peak deconvoluted into two peaks at 642.57 and 645.3 eV reveals the existence of Mn in +3 and +4 oxidation state, respectively. The approximate ratio between Mn^{3+} and Mn^{4+} present in δ-MnO_2 is calculated through XPS. The percentage of calculated Mn^{3+} and Mn^{4+} from $Mn2p_{3/2}$ spectrum is estimated to be 42.8% and 57.18%, respectively. The ratio of Mn^{3+} to Mn^{4+} is found to be ~ 0.75. Further, O 1s peak deconvoluted into two peaks at 529.89, and 531.83 eV are attributed to the peaks corresponding to lattice oxygen (O_a) and surface oxygen (O_b), respectively (figure 4.5 (b)). The area ratio of O_b to O_a is found to be 0.57 indicates the presence of oxygen vacancies in the synthesized sample.

4.3 Magnetic Properties

Temperature and magnetic field dependent magnetization, temperature dependent ac susceptibility, and time dependent remanant magnetization are carried out to investigate the magnetic properties of δ-MnO_2, and are discussed in sections 4.3.1, 4.3.2, 4.3.3, and 4.3.4, respectively.

4.3.1 Temperature Dependent Magnetization

Figure 4.6(a) depicts the temperature-dependent dc magnetization of δ-MnO_2 measured between 2 and 300K after zero-field cooling (ZFC) and field cooling (FC) process with an applied external magnetic field of 100 Oe. For ZFC mode, the sample is cooled down from 300 K to 2 K in the absence of a magnetic field whereas, for FC mode, the sample is cooled in the presence of an external magnetic field of 100 Oe. One can observe that, for δ-MnO_2, on decreasing temperature from 300 K, M_{ZFC} and M_{FC} curves do not show any bifurcation

up to M_{max} observed at 13.2 K (T_{irr}) (figure 4.6(b)) accompanied by a clear bifurcation below it. A sharp cusp is observed on both FC and ZFC curves at T_{max}, 10.6 K. However, both ZFC and FC curves become virtually identical above the magnetic transition temperature (13.2K) and show paramagnetic behaviour. Inverse susceptibility of ZFC magnetization in higher temperature regime (200 to 300 K) is fitted with Curie-Weiss law $1/\chi = (T-\theta_{cw})/C$ shown in figure 4.6(c). Curie-Weiss temperature, θ_{cw}, and Curie constant, C is found to be -288 K and 3.18 emuK/molOe, respectively. A negative Weiss constant, θ_{cw} is a signature of strong antiferromagnetic behaviour. From this fit, the average effective magnetic moment is determined using the following equation

$$\mu_{eff} = \sqrt{[3Ck_\beta / (N_A\mu_B^2)]} \tag{4.1}$$

where k_β s Boltzmann's constant and N_A is Avogadro's number [1]. The calculated value is found to be 5.076 μ_B which is higher than expected for the spin-only moment of Mn^{4+} (3.87 μ_B). Such a large magnetic moment could be due to the presence of Mn^{3+} ions in δ-MnO_2 which is having a large magnetic moment (4.90 μ_B) in the high spin state than that of Mn^{4+}. We have further determined quantitatively the fraction of Mn^{3+} ions using the following equation [162]

$$\mu_{eff}^2 = (1 - y) [\mu_{eff}(Mn^{4+})]^2 + y [\mu_{eff}(Mn^{3+})]^2 \tag{4.2}$$

where y denotes the concentration of Mn^{3+} which is found to be 0.84. On the basis of electrostatic charge neutrality, the presence of additional Mn^{3+} ions in the matrix gives the confirmation for the existence of oxygen vacancies in the sample. An oxygen vacancy is a result of two Mn^{3+} ions which gives an actual composition of MnO_2 as $MnO_{1.58}$.
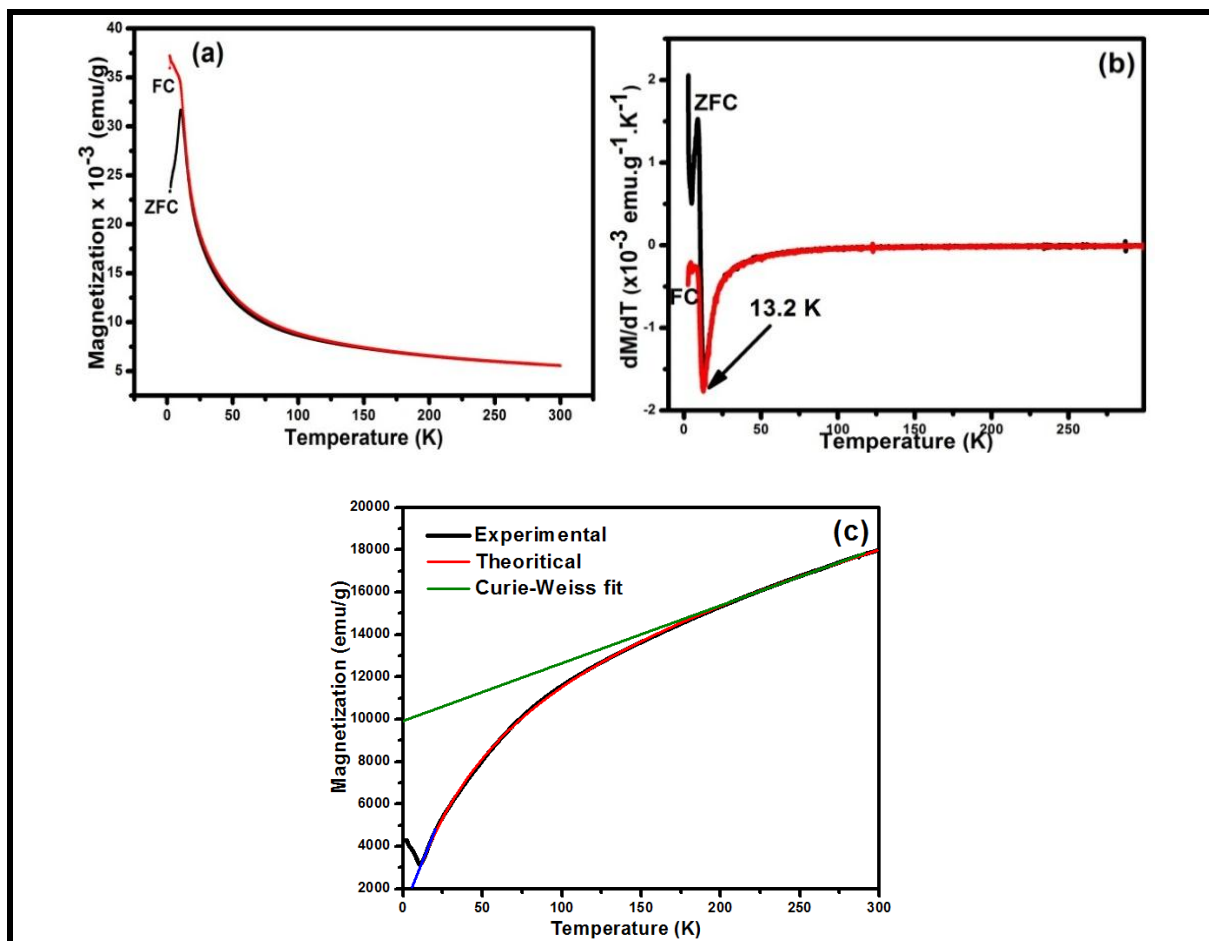
Figure 4.6: *(a) Temperature dependent magnetization (M-T) curve of δ-MnO₂ measured under applied field of 100 Oe. (b) shows the derivative dM/dT with temperature and (c) shows the inverse susceptibility versus temperature fitted with Curie-Weiss law in paramagnetic region.*

Although MnO_2 is antiferromagnetic in nature, because of the formation of the morphology, one may assume the presence of uncompensated spins at the surface of δ-MnO_2 resulting in ferrimagnetic ordering. Variation of reciprocal susceptibility (χ^{-1}) of paramagnetic range with temperature has been fitted with the following function (figure 4.6(a)) which consists of Curie-Weiss (ferrimagnetic) and Curie (paramagnetic) term [169].

$$\chi^{-1} = \frac{T}{C} + \frac{1}{\chi_0} - \frac{b}{T-\theta} \qquad\qquad [4.3]$$

The experimental data is completely fitted with this equation. Generally, the experimental data intersects the temperature axis at θ_f and the fitted equation cut at θ_p, called ferrimagnetic Curie point and paramagnetic Curie point, respectively. From the fitting, we observe that there is no difference between θ_f and θ_p which clearly confirms the strong antiferromagnetic behaviour of δ-MnO_2.

In general, the broad peak in M versus T and, the bifurcation in M_{FC} and M_{ZFC} below the maximum indicate the presence of spin-glass [179], canonical spin-glass [179][168][[169][170], cluster-glass [165] or superparamagnetic behavior [180][181]. At temperatures much below Tmax, M_{FC} increases with temperature, which violates the presence of canonical spin glass and therefore suggests that the system is probably a spin glass (SG), cluster glass (CG), or superparamagnetic (SPM) of either interacting or non-interacting nature. In order to attain more understanding of the magnetically ordered state in δ-MnO_2, we have commenced an ac susceptibility measurement at a low field and have discussed later. ZFC and FC magnetization curves measured at different applied fields are shown in the inset of figure 4.7(a,b). The maximum magnetization observed at T_{max} gradually shifts toward lower temperature with increasing magnetic field, which is consistent with a SG transition. In a SG system, the energy barrier can be suppressed by applying higher magnetic field, leading to a decrease in the freezing temperature. The field dependence of SG freezing temperature is explained on the basis of de Almeida-Thouless (AT) line [182][183]. The AT line can be observed near freezing temperature and associates with the onset of the irreversibility of spin-glasses. Field dependence of the SG freezing temperature is shown in figure 4.7(c) which follows the line as
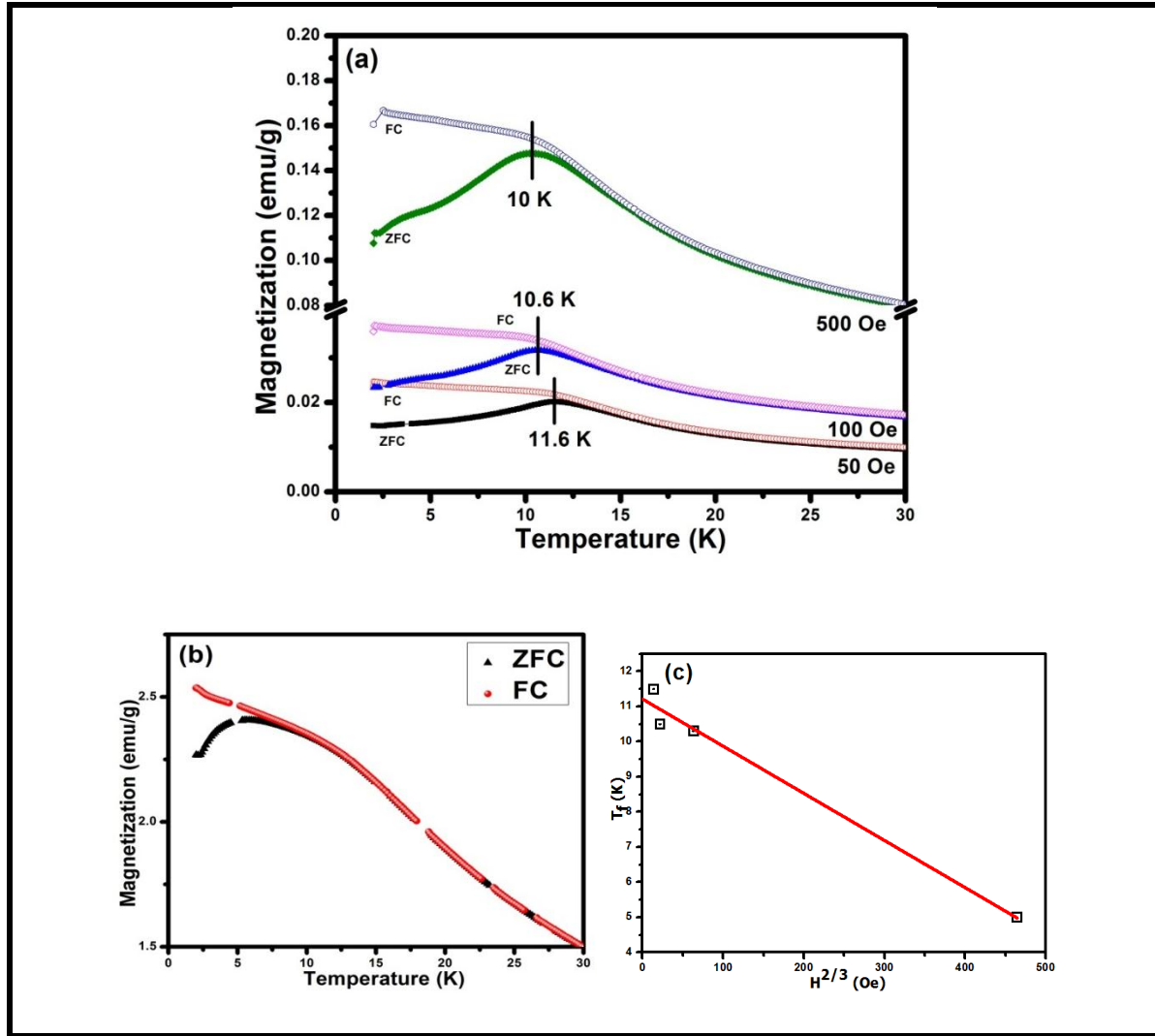
Figure 4.7: *Temperature dependent magnetization (M-T) curve of δ-MnO₂ measured under applied field of (a) 50, 100, 500 Oe, and (b) 10 kOe. (c) shows the field dependence of reduced temperature with the best fit in terms of A-T line.*

$$H^2 = A \left[1 - T_{max}(H)/T(0)\right]^3. \qquad\qquad [4.4]$$

where, $T_{max}(H)$ and $T(0)$ are the field-dependent and zero-field freezing temperatures, respectively [169]. Extrapolation of AT line at zero applied field determines the SG temperature which is found to be 11.2 K for δ-MnO₂. Generally, AT-like behavior is found

for SG systems which separate high temperature paramagnetic region with finite relaxation time from low temperature spin-glass phase with infinite relaxation time.

4.3.2 Field Dependent Magnetization

Further, we have examined the field-dependent magnetization measurement of δ-MnO$_2$ under ZFC condition at different temperatures (2K, 10K and 30K) in the range of ± 7 kOe without applying any external magnetic field as shown in figure 4.8(a). At 30 K, a linear increase in magnetization with the magnetic field confirms the paramagnetic phase of δ-MnO$_2$. At 2K, M vs. H exhibits a weak hysteresis loop of coercivity of 1.6 kOe with non-saturated magnetization, indicating the presence of weak ferromagnetic ordering. No loop observed at 10 K eliminates the weak ferromagnetic behavior. The similar unsaturated magnetic moment at 7 kOe has also been observed in α-K$_x$MnO$_2$ (x $\leq$ 0.125, =0.14) [6], [104], [184] and Ba$_{0.135}$MnO$_2$ [6] with hollandite type structure indicating the presence of both SG and antiferromagnetic phase. The finite coercivity at 2K may be attributed to the magnetic interaction between Mn^{3+} and Mn^{4+} ions present in δ-MnO$_2$ as confirmed from XPS. Besides the hysteresis observed at 2K under zero field cooling condition, we also observe shifting in hysteresis loop measured under FC condition at 2K with the application of 10 kOe magnetic field. However, shifting of the loop towards negative field direction indicates the presence of the exchange bias phenomenon (figure 4.8(b)). Exchange bias field determined from the formula, $H_{EB} = (Hc_1 + Hc_2)/2$ where Hc$_1$ and Hc$_2$ are the left and right coercive fields, respectively [185], is found to be 153 Oe for δ-MnO$_2$. Further, In order to obtain more understanding of the magnetically ordered state in δ-MnO$_2$, we have commenced an ac susceptibility measurement at a low field which probes the dynamics of the system at the timescale of the measuring frequency range.
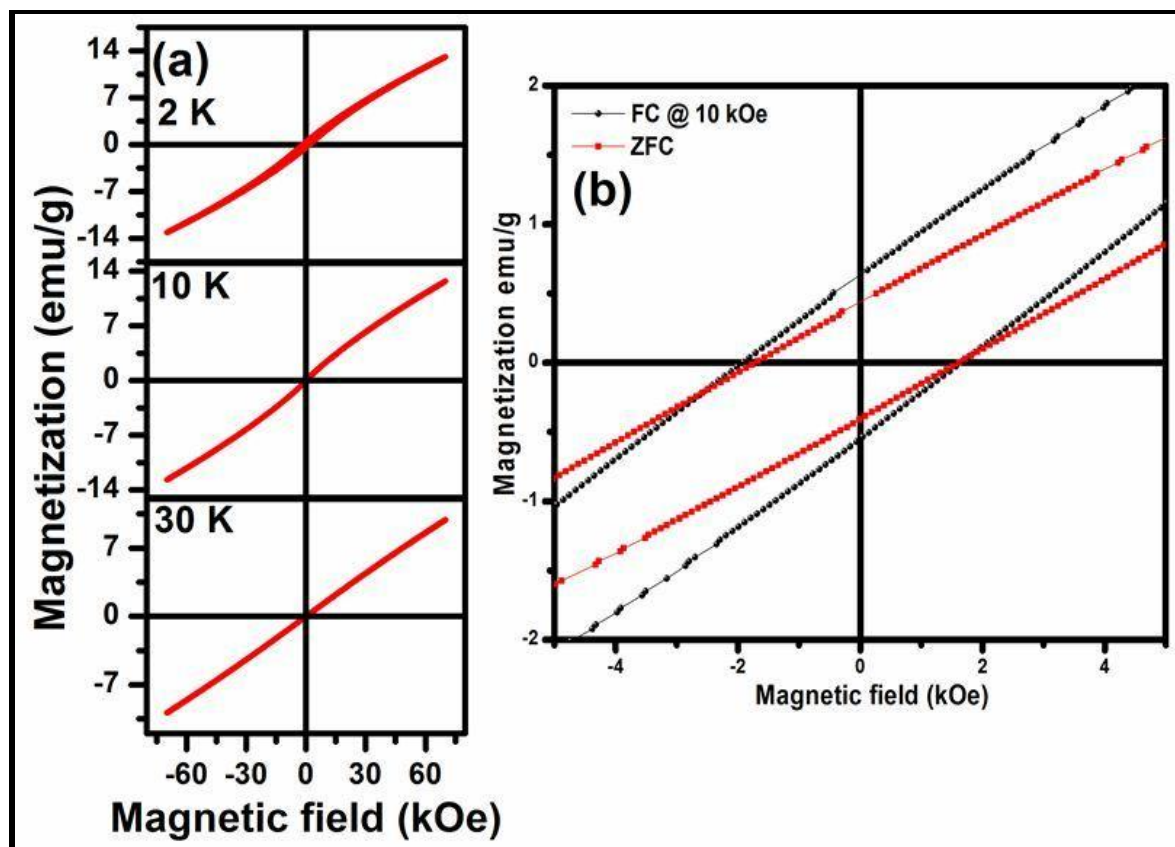
Figure 4.8: *(a) Magnetization vs. magnetic field at (a) 2, 10 and 30 K under ZFC and at (b) 2K under FC of δ-MnO$_2$.*

4.3.3 ac Susceptibility

Temperature-dependent real χ′ (T) and imaginary χ″ (T) of the ac-susceptibility at f=31, 101, 299, and 501 Hz is depicted in figure 4.9. One may notice from real χ′ (T) and imaginary χ″ (T) that a pronounced peak at freezing temperature, T$_f$~11.8 K, is observed at similar temperature observed from M$_{ZFC}$ measurement and from A-T line. There is a clear frequency dependence of the susceptibility in real χ′ (T) accompanied by a decrease in peak intensity and shift towards higher temperature with increasing frequency (inset of figure 4.9). Such dispersion behaviour of χ with frequency is a common feature in spin-glass,

cluster glass, and superparamagnetic system. In order to determine the nature of the magnetically ordered state and the strength of spin interaction, the frequency dependence of transition temperature, T_f, is fitted with the following relation (Mydosh parameter):

$$\phi = \Delta T_f / T_f \Delta(\log\omega) \qquad [4.5]$$

where ϕ is the relative frequency shift, Δ is the difference in related parameters, T_f is the spin freezing temperature at frequency ω [186]. It is usually between 0.005 and 0.08 for spin glass and interacting particle systems [187], 0.03-0.08 for cluster glass [166], and 0.1-0.13 for non-interacting superparamagnetic (SPM) particles [188]. In the present case, ϕ is found to be 0.027 which supports spin-glass and/or cluster glass freezing rather than superparamagnetic blocking. To verify the intercluster interaction and its effect on the fluctuation dynamics, different phenomenological models like the Neel–Arrhenius, Vogel–Fulcher and power law are verified. For an assembly of non-interacting SPM particles, relaxation time should follow the Neel-Arrhenius law without any critical behavior

$$\tau = \tau_o \exp\left(\frac{E_a}{K_B T}\right) \qquad [4.6]$$

where, E_a is the average anisotropy energy barrier equal to KV, K is the anisotropy constant and V is the volume of the particle [9]. The prefactor τ_o is the time constant corresponding to the inverse of characteristic frequency and K_B is the Boltzmann's constant. For SPM relaxation, τ_o depends on the gyromagnetic precession time and usually found in the range of $\sim 10^{-10}$ to 10^{-13} s. The best fitting of our data shown in figure 4.10(a) gives unphysical value i.e. $\tau_o \sim 1.252 \times 10^{-41} \ll 10^{-13}$ s which rules out the possibility of non-interacting SPM nature of the particles. Therefore, we express the interacting dynamics using Vogel-Fulcher law [189]

$$\tau = \tau_o \exp\left(\frac{-E_o}{K_B(T_f - T_o)}\right) \qquad [4.7]$$

where T_o is the characteristic SG transition temperature which accounts for interparticle interaction and has a value between 0 and T_f. The parameters, T_o, τ_o and E_a/K_b obtained by fitting (figure 4.10(b)) our data in equation 8 are determined as 10.43 ± 0.2 K, 4.7×10^{-9}s, and 19.87 eV, respectively.
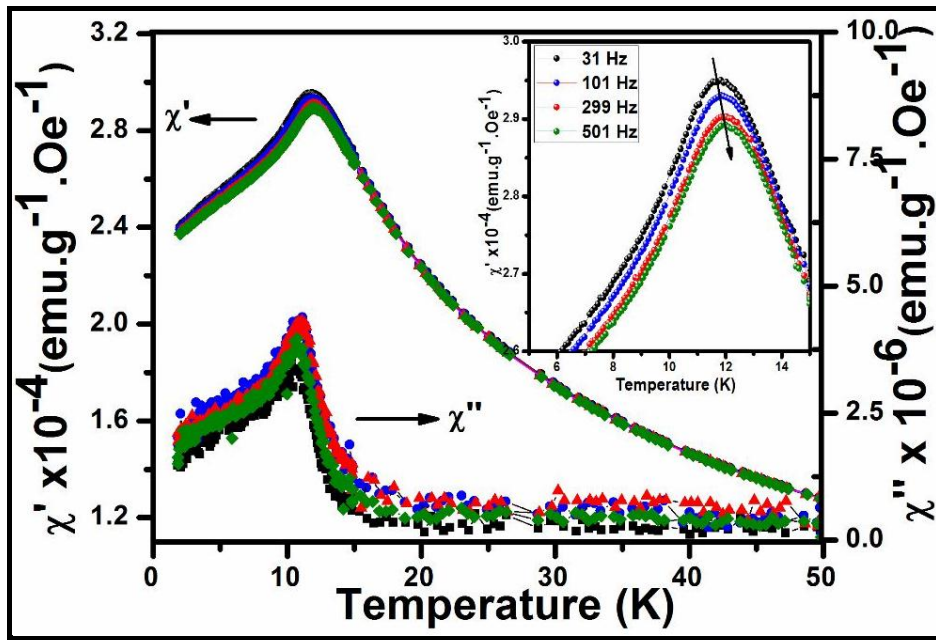

Figure 4.9: *Temperature dependence of real, $\chi^{'}$ and imaginary, $\chi^{''}$ of ac susceptibility at 31, 101, 299 and 501 with ac field of 3 Oe. The inset shows the enlarged view of the peak shift with frequency.*

The obtained value of τ_o is 10^{-9}s. Such a higher value of τ_o has been confirmed the interacting nature of particles which reveals cluster glass behavior as in cluster glass τ_o lies in the range of 10^{-6} to 10^{-10} s [166], [168], [190]. For SG system τ_o is typically within 10^{-11} to 10^{-13} s [191]. To further confirm the cluster-glass behaviour obtained from Vogel-

Fulcher law, frequency dependent shift of T_f can be fitted with Power law as well. The power law hypothesis assumes that the relaxation time (τ) is related to the correlation length (ξ) near the spin-glass transition temperature (T_{SG}). As ξ diverges at T_{SG}, relation time obeys following empirical relation [192]

$$\tau = \tau_o \left(\frac{T_f}{T_{SG}} - 1 \right)^{-z\upsilon} \qquad [4.8]$$

where z is the dynamic scaling exponent and υ is the critical exponent related to ξ. T_{SG} is the spin-glass freezing temperature in the limit of zero frequency. The parameters $T_{SG,}$ zυ, and τ_o, obtained from the best fit (inset of figure 4.10(c)) of the above equation demonstrates as 11.32 ± 0.03 K, 4.92 ± 0.8 and 1.62×10^{-9} s, respectively. For conventional spin-glass, τ_o lies between 10^{-10} to 10^{-13} s and zυ within 4 and 13 [193]. τ_o along with zυ obtained from Vogel-Fulcher and Power law confirm that the spin-glass nature is not atomic in origin, rather is related to clusters of atoms and hence we would identify it as a cluster glass. The cluster-glass behaviour results from the competition between the fero-antiferromagnetic interactions below Neel temperature, which is related to the intrinsic geometrical magnetic frustration present in the system. Such geometrical frustration could be due to the interaction between Mn^{3+} and Mn^{4+} present in δ-MnO_2. Similar cluster-glass behaviour has been reported in Mn rich $YMnO_3$ and Y doped $LaCa_{0.3}MnO_3$ [194][195].

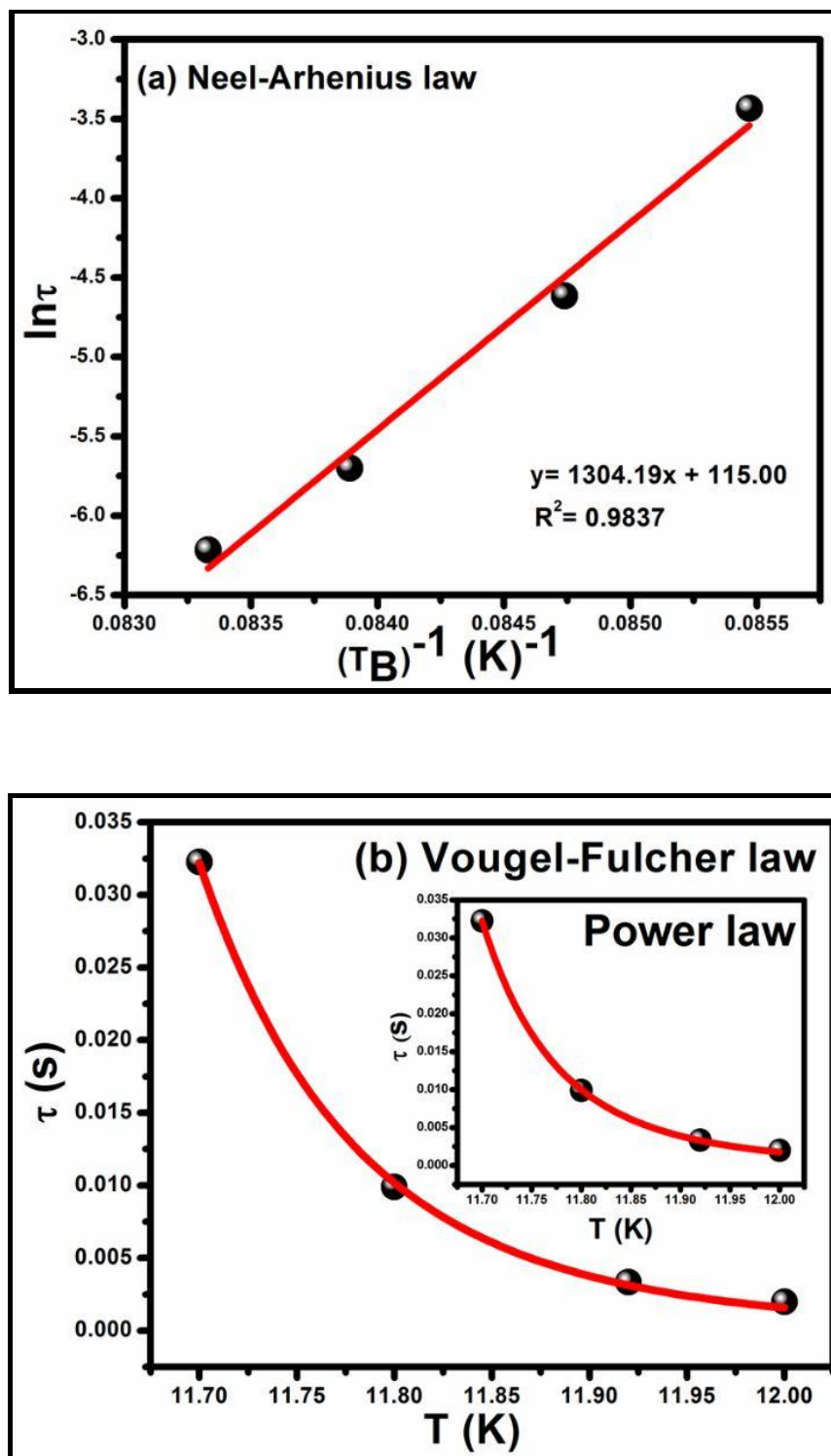*Figure 4.10:* *(a) Variation of relaxation time τ with temperature T_b plotted as lnτ versus $(T_b)^{-1}$ and fitted with Neel-Arrhenius law, (b) Vogel-Fulcher law and power law (inset).*

4.3.4 Remanant Magnetization Measurement

Further, remanent magnetization has been measured in FC mode with an applied field of 100 Oe at 5 K. Magnetization decay has been recorded as a function of time on the removal of the applied field after cooling the sample from 300K to 5K and wait for a certain time period, t_w as shown in figure 4.11(a). Remanent magnetization recorded across the whole experiment gives nonzero magnetization which decays very slowly i.e. less than 3% even after 13000 s. The decay behaviour reveals two regimes with different time responses. A rapid initial magnetization relaxation is followed by a slower relaxation. This longtime relaxation is unambiguously a feature of spin-glass dynamics [196]. According to theoretical and experimental studies, for a time shorter than 1500 s, SG relaxation displays power law decay (shown as inset) as mentioned below as equation (10) [171].

$$M(t) = M_0 t^{-\alpha} \qquad [4.9]$$

where M_0 is the initial magnetization at t=0 and α is the decay constant which signifies the decay rate. From the fit, we find a power law behavior for t < 1500 s as predicted by *Ulrich et.al.* It is also observed that the data is not fitted very well above 15000 s [196]. Alternatively, we attempted to fit the data to a logarithmic dependence used frequently to describe the relaxation process in the SG system with long-range magnetic order as (shown in the inset of figure 4.11(a))

$$M(t) = M_o(1-\alpha \ln t) \qquad [4.10]$$

where M_o is related to intrinsic ferromagnetic component and α depends on the strength of magnetic interactions. If the decay parameter is small enough then logarithmic decay can be obtained from power law decay [191]. Furthermore, M_{TRM} as a function of time could

be fitted with stretched exponential function which is the most popular function to describe

the SG and cluster SG dynamics of the system as (shown in figure 4.11(b))

$$M(t) = M_o + M_r \exp[-(t/\tau)^n] \qquad [4.11]$$

where τ is the characteristic relaxation time, M_r is related to the glassy component

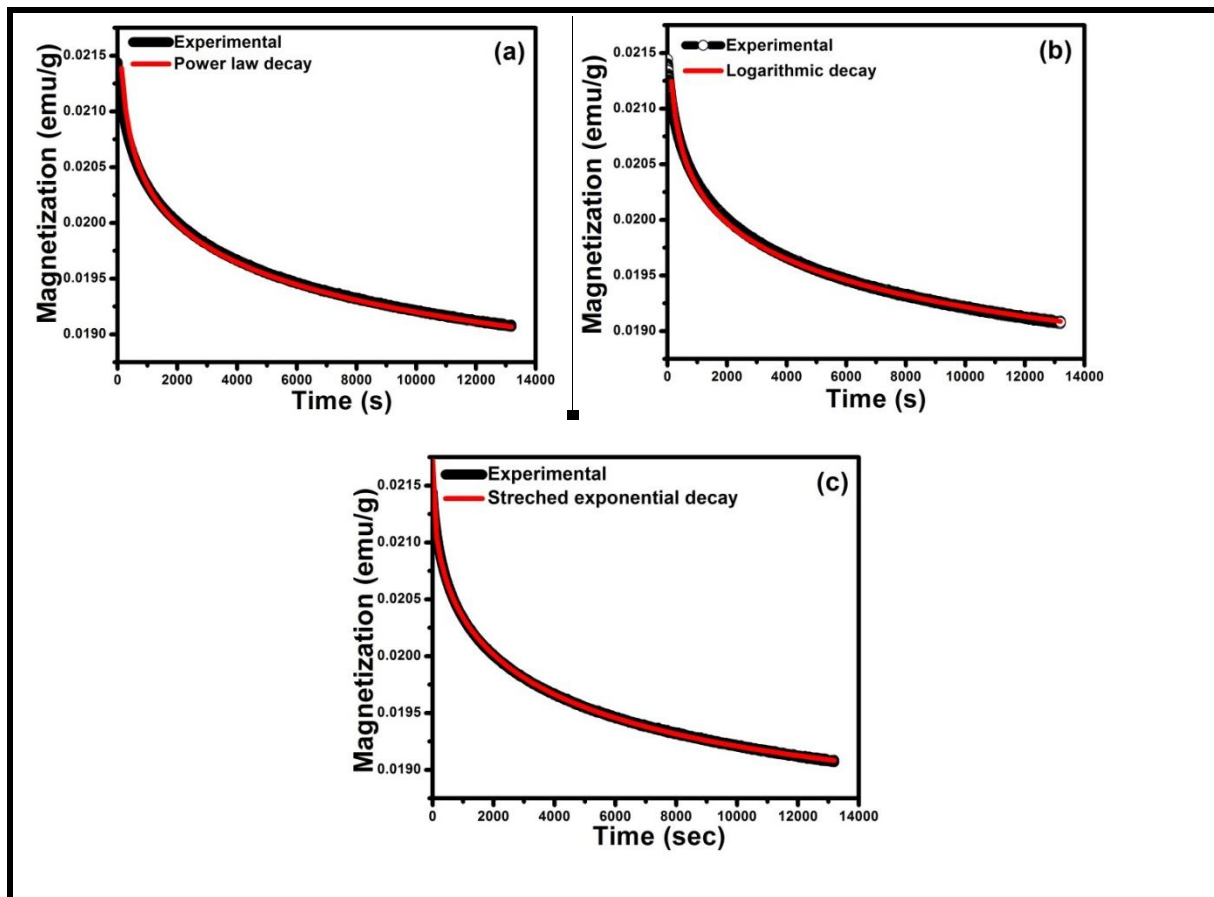contributing to the observed relaxation effect [193].

Figure 4.11: *Thermoremanent magnetization measurement at 5K fitted with (a) Power law, Logarithmic decay (inset) and (b) Stretched exponential decay functions.*

All the above three functions are important to describe the SG dynamics of the system, but it is still not understood that out of them which one is the most universal. Thus, from figure 4.11, we demonstrate that the time-dependent relaxation magnetization of δ-MnO$_2$ is explained approximately equally well with the power law, logarithmic decay function and stretched exponential function. Fitting parameters obtained from the above laws are tabulated in table 4.1. We observe that characteristic relaxation time, τ obtained from stretched exponential function displaying a similar decay tendency to those of power law and logarithmic functions. The observed exponent (n) and relaxation time (t) are in good agreement with the reported values corresponding to spin glass [168]. Spin-glass behaviour in Ba$_{1+\delta}$Mn$_8$O$_{16}$ is observed due to the presence of a complex interaction between the double chains of MnO$_6$ octahedra and a mixture between Mn^{4+} and Mn^{3+} as reported by *Yu et al.* [103]. *Luo et al.* observed spin-glass feature in α- MnO$_2$ attributed to the geometrical frustration in a triangular lattice and mixed valance of Mn^{4+} and Mn^{3+} [184].

Table 4.1: Fitting parameters deduced from thermo remanant relaxation magnetization fitted with empirical relations like power law decay, logarithmic decay and stretched exponential decay functions.

Sample	Power law decay		Logarithmic decay		Stretched exponential function			
	$M_\circ$ (emu/g)	α	$M_\circ$ (emu/g)	α	$M_\circ$ (emu/g)	M_r (emu/g)	T (s)	n
δ-MnO$_2$	0.0241	0.0249	0.02354	0.01995	0.01848	0.00324	3957.99	0.4287

Thus, antiferromagnetic δ-MnO$_2$ exhibit spin glass relaxation at low temperature which is contributed by the interaction between Mn^{4+} and Mn^{3+} present in δ-MnO$_2$. The weak ferromagnetism with finite coercivity observed below T$_f$ may be related to the intrinsic magnetic frustration in this system.

4.4 Conclusion

In summary, chapter includes the synthesis of bernessite structure of δ-MnO$_2$ through facile hydrothermal technique without using any template. XRD, FT-IR and Raman spectroscopy confirmed the formation of the δ phase of MnO$_2$. We studied the dynamic magnetic properties of δ-MnO$_2$ by carrying out dc magnetization, frequency-dependent ac susceptibility, and magnetic relaxation measurements. While dc magnetization showed the existence of AT type phase boundary with freezing of spin clusters at 11.2 K, frequency-dependent ac susceptibility predicted the freezing of interacting spin clusters. Frequency-dependent ac susceptibility analyzed using both Vogel-Fulcher law as well as power law, demonstrated the relaxation time constant, τ_o and interaction parameter, T$_o$ as 4.7 x 10^{-9} s, 10.43 $\pm$ 0.2 K and 1.62 x 10^{-9} s, 11.32 $\pm$ 0.03 K, respectively. Higher τ_o compared to that of conventional spin-glass clearly recommended the presence of clusters in this system. Below freezing temperature, remanent magnetization measurement confirmed the spin-glass behavior. The occurrence of the low temperature freezing of spin clusters was attributed to the complexity of the mixture of Mn^{3+}/Mn^{4+} with strong magnetic frustration in δ-MnO$_2$.